

Intention-Aware Planner for Robust and Safe Aerial Tracking

Qiuyu Ren, Huan Yu, Jiajun Dai, Zhi Zheng, Jun Meng and Li Xu

Abstract— The intention of the target can help us to estimate its future motion state more accurately. This paper proposes an intention-aware planner to enhance safety and robustness in aerial tracking applications. Firstly, we utilize the Mediapipe framework to estimate target’s pose. A risk assessment function and a state observation function are designed to predict the target intention. Afterwards, an intention-driven hybrid A* method is proposed for target motion prediction, ensuring that the target’s future positions align with its intention. Finally, an intention-aware optimization approach, in conjunction with particular penalty formulations, is designed to generate a spatial-temporal optimal trajectory. Benchmark comparisons validate the superior performance of our proposed methodology across diverse scenarios. This is attributed to the integration of the target intention into the planner through coupled formulations.

I. INTRODUCTION

With the advancement of unmanned aerial vehicle (UAV) technologies, aerial auto-tracking has found extensive applications in photography, rescue and inspection. An outstanding tracker should be capable of maintaining an appropriate distance and field of view (FOV) with the target. Meanwhile, it needs to have the ability to handle unexpected situations, such as sudden turns or decelerations of the target. Some state-of-the-art trackers [1]–[6] place great emphasis on visibility, safety, and trajectory smoothness, which demonstrates impressive robustness. However, these methods only utilize the target’s position, velocity, etc., for planning, while disregarding its high-dimensional semantic information such as intention. In fact, sudden alterations in the target intention can readily induce tracking failures. For instance, if the target turns abruptly at the corner, it can be occluded by obstacles easily. Hence, it is crucial to enable the tracker to be aware of the target intention. But most existing intention prediction methods are data-driven, which makes it challenging to model intentions into the planner.

In light of the aforementioned issues, we propose an intention-aware planner to improve robustness and safety in aerial tracking. Our framework incorporates three parts: intention prediction, motion prediction and trajectory optimization. In the first part, we utilize the Mediapipe framework to detect the target and then estimate its position, velocity and rotation. After that, we design a risk assessment function and a state observation function to predict the target intention.

Corresponding Author: Li Xu, xupower@zju.edu.cn

This work was supported by Robotics Institute of Zhejiang University under Grant K12106 and K11801.

All authors are with the College of Electrical Engineering, Zhejiang University, Hangzhou 310027, China, and also with the Robotics Institute of Zhejiang University, Yuyao 315400, China.

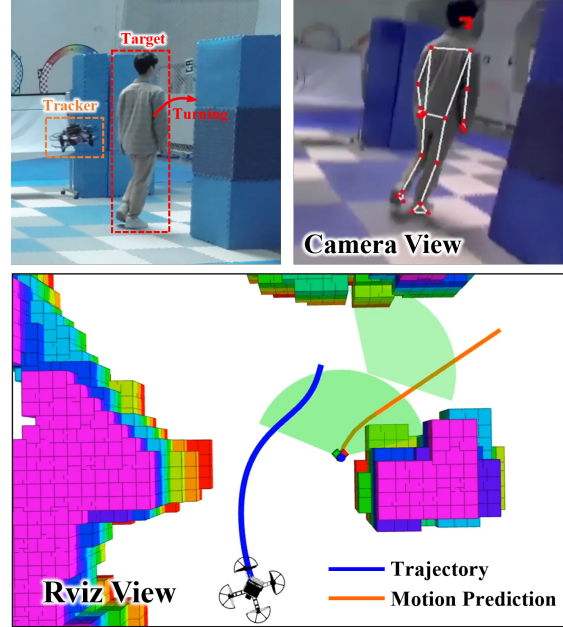


Fig. 1. The real-world performance of our method. The target makes a sharp turn at the intersection and our tracker can predict its intention to plan an adequate trajectory.

As for target motion prediction, we propose an intention-driven hybrid A* method that expands nodes by generating intention primitives. Each kind of primitive is driven by one singular intention. Subsequently, we design a penalty matrix to describe the penalty of intention transition. By exploring a path with the least cost, we can obtain target’s future positions that adheres to its intention. Finally, an intention-aware optimization approach is employed to generate a spatial-temporal optimal trajectory. Particular penalty formulations are designed to enable the tracker to cope with different target intentions flexibly. Experimental results demonstrate that combining the target intention with planning greatly improves the robustness and safety of tracking.

Our main contributions are summarized as follows:

- 1) A flexible intention prediction method that integrates user-defined risk assessment function and state observation function.
- 2) An intention-driven target motion prediction approach that estimates target’s future positions by generating intention primitives.
- 3) An intention-aware trajectory optimization method to generate a spatial-temporal optimal trajectory by designing particular penalty formulations.
- 4) Simulated and Real-world experiments are conducted to validate the robustness and safety of our method.

II. RELATED WORK

Some previous UAV trackers [7]–[9] can achieve real-time tracking, but they all take the deviation of the target on the image space as the feedback of the controller and ignore the surrounding obstacles, which restricts them to running in open areas. In recent years, some state-of-the-art UAV tracking controller [1]–[6] have taken safety, visibility and smoothness into account which makes trackers be capable of tracking targets robustly and efficiently in cluttered environments. Han et al. [2] propose Fast-Tracker, which consists of a target informed trajectory prediction front-end as well as a spatial-temporal optimal and collision-free trajectory generation back-end, equipping the tracker with high mobility in dense environments. Wang et al. [3] propose a visibility-aware trajectory optimization method that lays high emphasis on the visibility of targets. By formulating the metric into a differentiable visibility cost function, targets can be observed better in complicated environments. Ji et al. [5] propose Elastic-Tracker. They design a smart occlusion-aware path finding method and an effective trajectory optimization approach to keep the tracker at an appropriate distance from the target, enabling the tracker to cope with unexpected situations and realizing elastic tracking. However, none of them takes the target intention into consideration.

Human intention prediction is widely applied in pedestrian crossing and human-robot interaction scenarios, which can be divided into two categories: neural network-based and probabilistic model-based. The former includes MLP [10, 11], CNN [12], LSTM [13], etc., while the latter includes HMM [14], DBN [15], CRF [16, 17], etc. Alahi et al. [18] constitute an LSTM architecture for modeling interactions and predicting trajectories of multiple agents in crowded spaces. A distinct social pooling layer simulates interpersonal relationships by aggregating hidden states of neighboring pedestrians. This approach captures complex human-human interactions to render accurate multi-agent trajectory forecasting. Schulz et al. [17] develop a Latent-dynamic Conditional Random Field (LDCRF) model that integrates pedestrian dynamics and situational awareness. The model is able to capture both intrinsic and extrinsic class dynamics and shows great stability. Nevertheless, these methods are all data-driven which lack generalization and are not lightweight enough.

III. TARGET INTENTION PREDICTION

A. Human Pose Estimation and Localization

Human pose estimation is performed using the Mediapipe framework, shown in Fig. 2. Mediapipe is an open-source toolkit developed by Google for building multimodal perception pipelines. The pose estimation module utilizes the BlazePose [19] framework to estimate 33 3D joint landmarks, both 2D landmarks $p_n^i \in \mathbb{R}^2$ in the image frame and 3D landmarks $p_n^h \in \mathbb{R}^3$ in the human body frame, with high accuracy and real-time performance. To localize the target, we select four sets of joint coordinates $\{p_{11}^i, p_{11}^h\}, \{p_{12}^i, p_{12}^h\}, \{p_{23}^i, p_{23}^h\}, \{p_{24}^i, p_{24}^h\}$, namely left

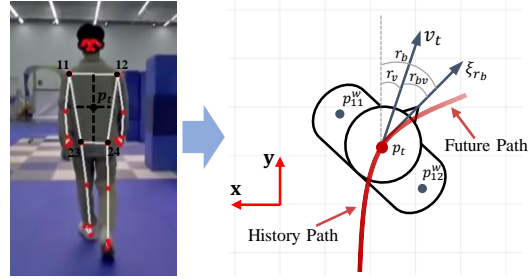


Fig. 2. Target localization and pose estimation.

shoulder, right shoulder, left hip and right hip, and determine their 3D coordinates in the camera frame by solving the Perspective-n-Points algorithm. We can obtain their world frame coordinates $\{p_{11}^w, p_{12}^w, p_{23}^w, p_{24}^w\}$ through coordinate transformation. Then the target's world frame coordinate can be presented as

$$p_t^w = (p_{11}^w + p_{12}^w + p_{23}^w + p_{24}^w)/4, \quad (1)$$

which is abbreviated as $p_t = P_t(t)$ in the following sections. Afterwards, we utilize an EKF with CV (Constant Velocity) model to estimate its velocity $v_t = V_t(t)$. Then, we define the target's body rotation vector as

$$\xi_{r_b} = [p_{11}^w(2) - p_{12}^w(2), p_{11}^w(1) - p_{12}^w(1), 0]^T. \quad (2)$$

The body rotation angle $r_b \in [-\pi, \pi]$ and velocity angle $r_v \in [-\pi, \pi]$ can be described as

$$\begin{cases} r_b = \tan^{-1}[\xi_{r_b}(0)/\xi_{r_b}(1)], \\ r_v = \tan^{-1}[v_t(0)/v_t(1)]. \end{cases} \quad (3)$$

Finally, the angle $r_{bv} \in [-\pi, \pi]$ between ξ_{r_b} and v_t can be calculated as

$$r_{bv} = \begin{cases} (r_b - r_v) + 2\pi, & r_b - r_v < -\pi, \\ r_b - r_v, & -\pi \leq r_b - r_v \leq \pi, \\ (r_b - r_v) - 2\pi, & r_b - r_v > \pi, \end{cases} \quad (4)$$

where $r_{bv} > 0$ when ξ_{r_b} is on the left side of v_t , otherwise $r_{bv} < 0$.

B. Reachable Region Generation

Human's movement intention is closely related to its motion state and the surrounding environment. We introduce a sector-shaped reachable region $\mathcal{R}(t) = \mathcal{R}_l(t) \cup \mathcal{R}_r(t)$ to describe the area that the target will most possibly reach within 1s at time t :

$$\begin{cases} \mathcal{R}_l(t) = \left\{ x \in \mathbb{R}^3 \mid \langle x - P_t(t), \xi_l(t) \rangle \leq \theta_l(t) \right\}, \\ \mathcal{R}_r(t) = \left\{ x \in \mathbb{R}^3 \mid \langle x - P_t(t), \xi_r(t) \rangle \geq \theta_r(t) \right\}, \end{cases} \quad (5)$$

where $0 \leq \theta_l(t), \theta_r(t) \leq \pi/2$. $\mathcal{R}_l(t)/\mathcal{R}_r(t)$ denotes the left/right reachable region of the target, $\theta_l(t)/\theta_r(t)$ is the corresponding angle of the sector.

As shown in Fig. 3, $\mathcal{R}_l(t)$ and $\mathcal{R}_r(t)$ are separated by the velocity vector $V_t(t)$, and the reachable region is larger on the side that is further from obstacles in the direction of $V_t(t)$. We can obtain $P_t(t+t_0)$ and $V_t(t+t_0)$ using the CV model to estimate $\mathcal{R}(t+t_0)$.

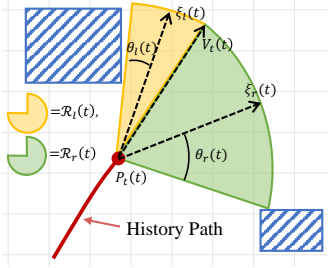


Fig. 3. Reachable region generation.

C. Target Intention Prediction

Given the target's intention set $\mathcal{I} = \{i_1, i_2, \dots, i_{m_i}\}$, we introduce an intention prediction function to evaluate the probability of each intention $i \in \mathcal{I}$:

$$I_i^p(t) = \varphi[I_i^r(t), I_i^o(t)], \quad (6)$$

where $I_i^p(t) \in [0, 1]$ describes the occurring probability of intention i at time t . $I_i^r(t)$ is a risk assessment function, describing the potential risk of i . $I_i^o(t)$ is a state observation function which serves as direct evidence for i . $I_i^r(t)$ and $I_i^o(t)$ differ for different $i \in \mathcal{I}$, and users can customize them as needed. $\varphi[\cdot]$ is an activation function.

In this paper, we consider four kinds of intentions, namely constant velocity, turning left, turning right and deceleration, described as $\mathcal{I}_0 = \{i_{cv}, i_{tl}, i_{tr}, i_{dec}\}$.

For turning intentions i_{tl} and i_{tr} , we pay particular attention when the target moves along obstacles and approaches a corner, due to the fact that the target is prone to being occluded by obstacles in tracker's FOV if it makes a sharp turn at the corner. Moreover, we notice that target's left/right reachable region increases when it approaches a left/right corner. In other words, the risk of i_{tl}/i_{tr} increases when θ_l/θ_r becomes larger. Based on this fact, we define $I_{i_{tl}}^r(t)$ and $I_{i_{tr}}^r(t)$ as

$$\begin{cases} I_{i_{tl}}^r(t) = \max\{k_1(\theta_l(t + t_0) - \theta_l(t)), 0\}, \\ I_{i_{tr}}^r(t) = \max\{k_1(\theta_r(t + t_0) - \theta_r(t)), 0\}, \end{cases} \quad (7)$$

where k_1 is a scaling factor and t_0 is a time constant.

When a person turns, $|r_{bv}|$ will increase suddenly. Therefore, we define $I_{i_{tl}}^o(t)$ and $I_{i_{tr}}^o(t)$ as

$$\begin{cases} I_{i_{tl}}^o(t) = \max\{k_2(r_{bv}), 0\}, \\ I_{i_{tr}}^o(t) = \max\{-k_2(r_{bv}), 0\}. \end{cases} \quad (8)$$

As for intention i_{dec} , the closer the target approaches the front obstacles and the greater its velocity, the higher the risk that it will decelerate. So we define $I_{i_{dec}}^r(t)$ as

$$I_{i_{dec}}^r(t) = k_3(\|V_t(t)\|^2/d_o), \quad (9)$$

where d_o is the distance to the nearest obstacle in the direction of $V_t(t)$.

We use the decrease of $\|V_t(t)\|$ within the time interval Δt to evaluate $I_{i_{dec}}^o(t)$:

$$I_{i_{dec}}^o(t) = \max\{k_4(\|V_t(t - \Delta t)\| - \|V_t(t)\|), 0\}. \quad (10)$$

As a normal motion intention, i_{cv} is evaluated based on the other unexpected intentions:

$$\begin{cases} I_{i_{cv}}^r(t) = -k_4 \max\{I_{i_{tl}}^r(t), I_{i_{tr}}^r(t), I_{i_{dec}}^r(t)\} + b_1, \\ I_{i_{cv}}^o(t) = -k_5 \max\{I_{i_{tl}}^o(t), I_{i_{tr}}^o(t), I_{i_{dec}}^o(t)\} + b_2, \end{cases} \quad (11)$$

where b_1 and b_2 are constant values.

Finally, $I_i^p(t)$ is expressed as

$$I_i^p(t) = \frac{\tanh[I_i^r(t) + I_i^o(t) - b_0] + 1}{2}, \quad (12)$$

where b_0 is a tunable parameter to control the sensitivity of the prediction.

IV. INTENTION-DRIVEN TARGET MOTION PREDICTION

Target motion prediction is achieved through node expansions. Conventional hybrid A* algorithm [20] expands nodes by generating motion primitives which fails to reflect target intentions. We propose an intention-driven hybrid A* algorithm, endowing each node with one target intention to generate intention primitives.

We define a key vector $\mathbf{i}_k = [i_1, i_2, \dots, i_{m_i}]^T \in \mathbb{R}^{m_i}$ for intentions in \mathcal{I} . Each node n possesses a state vector $x_n = [p_n^T, v_n^T]^T \in \mathbb{R}^6$, an intention value (value vector) $i_{vn} \in \mathcal{I}$ and the corresponding intention vector (query vector) $i_{qn} = e_i \in \mathbb{R}^{m_i}$, where

$$i_{vn} = i_{qn}^T \mathbf{i}_k, \quad (13)$$

i_{vn} denotes the intention input to node $n - 1$ and each i_{vn} corresponds to a physical model to generate the intention primitive. Taking \mathcal{I} as the input set, each node will expand $m_i \times m_0$ intention primitives, where m_0 is the number of primitives for each intention. The state of the initial node is set to the target's current state $x_0 = [p_t^T, v_t^T]^T$ and i_{v0} is set to intention i with the max $I_i^p(t)$.

We expect to find a path with the least change in the target intention within the prediction time T_p and define a penalty matrix $I_{pen} \in \mathbb{R}^{m_i \times m_i}$, where $I_{pen}(i_1, i_2)$ represents the cost of the transition from intention $\mathbf{i}_k(i_1)$ to $\mathbf{i}_k(i_2)$ ($0 \leq i_1, i_2 < m_i$). If $i_1 = i_2$ then $I_{pen}(i_1, i_2) = 0$, otherwise $I_{pen}(i_1, i_2) > 0$.

As a result, we designed both cost function $f(n)$ and heuristic function $h(n)$ as

$$f(n) = g(n) + h(n), \quad (14)$$

$$g(n) = i_{qn-1}^T I_{pen} i_{qn}, \quad (15)$$

$$h(n) = w_h d_{xy}[p_n, P_t(t + T_p)], \quad (16)$$

TABLE I
STATE TRANSITION EQUATIONS.

Intention	Model	State transition equations
i_{cv}	CV	$p_n = p_{n-1} + v_{n-1} \Delta t$ $p_n(0) = v_{n-1}(0) \frac{\sin(w\Delta t)}{w} + v_{n-1}(1) \frac{\cos(w\Delta t) - 1}{w}$
i_{tl}/i_{tr}	CT	$p_n(1) = v_{n-1}(0) \frac{1 - \cos(w\Delta t)}{w} + v_{n-1}(1) \frac{\sin(w\Delta t)}{w}$ $v_n(0) = v_{n-1}(0) \cos(w\Delta t) - v_{n-1}(1) \sin(w\Delta t)$ $v_n(1) = v_{n-1}(0) \sin(w\Delta t) + v_{n-1}(1) \cos(w\Delta t)$
i_{dec}	CA	$p_n = p_{n-1} + v_{n-1} \Delta t + 0.5a\Delta t^2$ $v_n = v_{n-1} + a\Delta t$

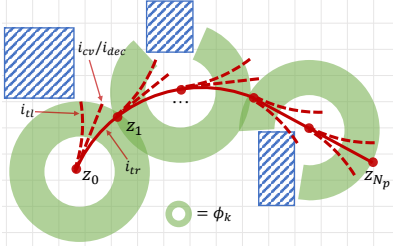


Fig. 4. A target motion prediction example when the target turns right.

where $P_t(t + T_p) = P_t(t) + V_t(t)T_p$. $d_{xy}(p_1, p_2)$ represents the horizontal distance between p_1 and p_2 . w_h is a weight term.

In this paper, we take \mathcal{I}_0 as the input set ($m_i = 4$), and the state transition equations are shown in Tab. I. By finding a minimum-cost path, we obtain a series of target future positions (shown in Fig. 4) as well as the corresponding time stamps, denoted by

$$\begin{cases} \mathcal{Z} = \left\{ z_k \in \mathbb{R}^3 \mid 0 < k \leq N_p \right\}, \\ \mathcal{T} = \left\{ t_k \in (0, T_p] \mid 0 < k \leq N_p \right\}. \end{cases} \quad (17)$$

Afterwards, we follow Ji's [5] work setting an occlusion-free region ϕ_k for each $z_k \in \mathcal{Z}$ and finding N_p A* paths passing through $\phi_1, \phi_2, \dots, \phi_{N_p}$. Letting s_k denote the endpoint of the k -th A* path, s_1, s_2, \dots, s_{N_p} are set as the initial tracking waypoints.

V. INTENTION-AWARE TRAJECTORY OPTIMIZATION

A. Trajectory Parameterization

In this paper, we utilize the trajectory class $\mathfrak{T}_{\text{MINCO}}$ [21] for trajectory parameterization and optimization, which is defined as

$$\begin{aligned} \mathfrak{T}_{\text{MINCO}} = & \left\{ p(t) : [0, T] \mapsto \mathbb{R}^m \mid \mathbf{c} = \mathcal{M}(\mathbf{q}, \mathbf{T}), \right. \\ & \left. \mathbf{q} \in \mathbb{R}^{m(M-1)}, \mathbf{T} \in \mathbb{R}_{>0}^M \right\}, \end{aligned}$$

where $p(t)$ is an m -dimensional polynomial trajectory of $N = 2s - 1$ order and M pieces. $\mathbf{q} = [q_1, q_2, \dots, q_{M-1}]$ are the intermediate waypoints. $\mathbf{T} = [T_1, T_2, \dots, T_M]^T$ and $\mathbf{c} = [\mathbf{c}_1^T, \mathbf{c}_2^T, \dots, \mathbf{c}_M^T]^T \in \mathbb{R}^{2Ms \times m}$ are the durations and coefficients of the trajectory pieces. The i -th piece in $\mathfrak{T}_{\text{MINCO}}$ is denoted by

$$p_i(t) = \mathbf{c}_i(t)^T \beta(t), \quad (18)$$

where $\beta(t) = [1, t, \dots, t^N]^T$ is the natural basis.

The function \mathcal{M} enables computing \mathbf{c} from \mathbf{q} and \mathbf{T} with linear complexity, which allows any second-order continuous cost function $\mathcal{J}(\mathbf{c}, \mathbf{T})$ with available gradient applicable to $\mathfrak{T}_{\text{MINCO}}$. As a result, by calculating $\partial \mathcal{J} / \partial \mathbf{c}$ and $\partial \mathcal{J} / \partial \mathbf{T}$, the gradients on the trajectory coefficients and times can be efficiently backpropagated to \mathbf{q} and \mathbf{T} with linear time complexity.

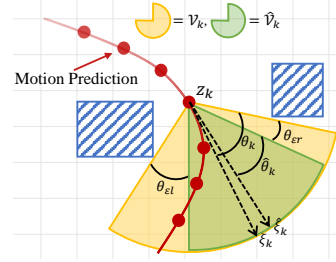


Fig. 5. Desired visible region generation.

We construct $\mathcal{J}(\mathbf{c}, \mathbf{T})$ as a multi-objective optimization cost function:

$$\begin{aligned} \lim_{\mathbf{q}, \mathbf{T}} \mathcal{J}(\mathbf{c}, \mathbf{T}) = & \mathcal{J}_s(\mathbf{c}, \mathbf{T}) + \sum_{*} \sum_{i=1}^M \mathcal{J}_s^*(\mathbf{c}_i, T_i) \\ & + \sum_{*} \sum_{k=1}^{N_p} \mathcal{J}_a^*(\mathbf{c}_j, t_k), \end{aligned} \quad (19)$$

where \mathcal{J}_s is the smoothness term, for which we employ the minimum jerk cost ($s = 3$). The last two terms correspond to the relative time penalty and absolute time penalty, respectively, which will be elaborated in the subsequent sections.

B. Relative Time Penalty

Following the approach of Liu et al. [22], the flight corridors are first generated as a series of polytopes:

$$\mathcal{F} = \bigcup_{i=1}^{M_{\mathcal{F}}} \mathcal{F}_i, \mathcal{F}_i = \left\{ x \in \mathbb{R}^3 \mid \mathbf{A}_i x \leq b_i \right\}, \quad (20)$$

where $M = KM_{\mathcal{F}}$ indicates that each flight corridor contains K trajectory pieces ($K = 2$ in this paper).

Then the collision avoidance constraints and dynamics constraints can be described as

$$\begin{cases} \mathcal{G}_f = \mathbf{A}_{[i/K]} p_i(t) - b_{[i/K]} \leq 0 & \forall t \in [0, T_i], \\ \mathcal{G}_v = \|p_i^{(1)}(t)\|^2 - v_{\max}^2 \leq 0, & \forall t \in [0, T_i], \\ \mathcal{G}_a = \|p_i^{(2)}(t)\|^2 - a_{\max}^2 \leq 0, & \forall t \in [0, T_i], \end{cases} \quad (21)$$

where $1 \leq i \leq M$. \mathcal{G}_* can be further transformed into the relative time penalty via the time integral method [23]:

$$\mathcal{J}_r^*(\mathbf{c}_i, T_i) = \frac{T_i}{\kappa_i} \sum_{j=0}^{\kappa_i} \bar{\omega}_j \max\{\mathcal{G}_*(\mathbf{c}_i, T_i, \frac{j}{\kappa_i}), 0\}^3, \quad (22)$$

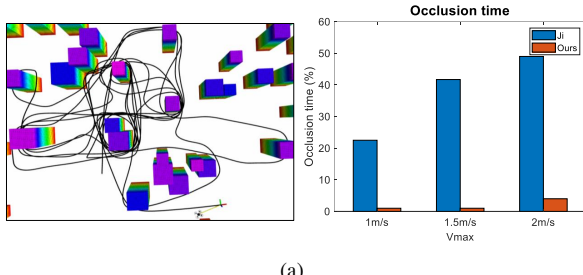
where $[\omega_0, \omega_1, \dots, \omega_{\kappa_i-1}, \omega_{\kappa_i}] = [\frac{1}{2}, 1, \dots, 1, \frac{1}{2}]$ are the quadrature coefficients resulting from the trapezoidal rule, $* = \{f, v, a\}$.

C. Absolute Time Penalty

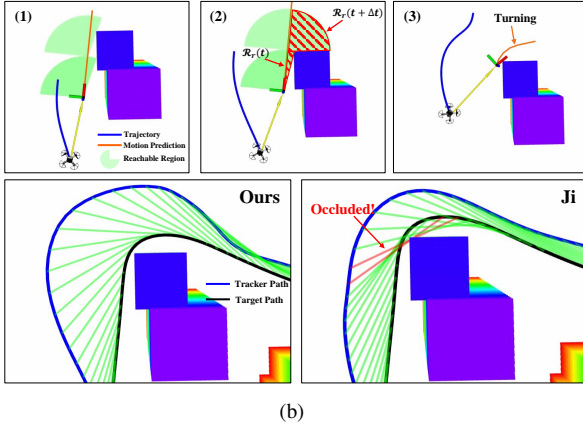
The absolute time penalty is enforced with the prediction time t_k , where t_k resides on the j -th piece of the trajectory:

$$p(t_k) = \mathbf{c}_j^T \beta(t_k - \sum_{i=1}^{j-1} T_i), \sum_{i=1}^{j-1} T_i \leq t_k \leq \sum_{i=1}^j T_i. \quad (23)$$

For each target future position $t_k \rightarrow z_k$, we hope $p(t_k)$ and z_k to maintain suitable distance and adequate visibility.



(a)



(b)

Fig. 6. (a) The target executes multiple sharp turns in a dense environment. Left: target's history path. Right: occlusion time of the two methods at different target velocity. (b) Top: the motion process of our tracker in one specific turn. Bottom: the history path of the two trackers during the turn.

1) *Distance Constraints*: Given a desired distance d_0 , we hope that the horizontal distance between the tracker and target is maintained within $[d_0 - d_l, d_0 + d_u]$, where $d_l, d_u = d_\tau$ represents the lower and upper tolerance distance. To further augment safety, more stringent requirements are imposed on d_l when the target exhibits deceleration trends:

$$d_l = (1 - I_{i_{dec}}^p(t))d_\tau. \quad (24)$$

Then the distance constraints can be written as

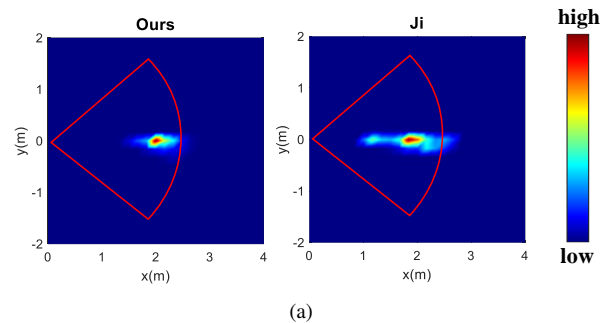
$$\begin{cases} \mathcal{G}_{d_l} = (d_0 - d_{xy}[p(t_k), z_k]) - d_l \leq 0, & \forall 1 \leq k \leq N_p, \\ \mathcal{G}_{d_u} = (d_{xy}[p(t_k), z_k] - d_0) - d_u \leq 0, & \forall 1 \leq k \leq N_p, \end{cases} \quad (25)$$

2) *Visibility Constraints*: Ji et al. [5] generate a visible region \mathcal{V}_k for each z_k . As shown in Fig. 5, to ensure the visibility of the target, we leave margin angles $\theta_{\varepsilon l}$ and $\theta_{\varepsilon r}$ that are related to $I_{i_{tl}}^p(t)$ and $I_{i_{tr}}^p(t)$ on both sides of \mathcal{V}_k :

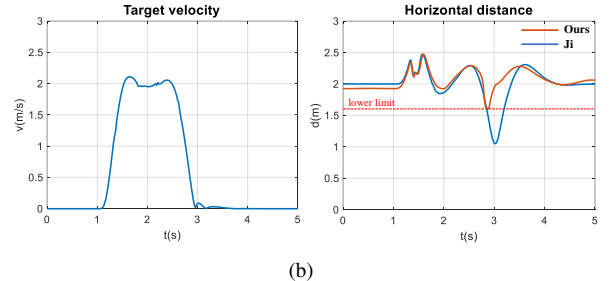
$$\begin{cases} \theta_{\varepsilon l} = \theta_\alpha + \theta_\beta I_{i_{tl}}^p(t), \\ \theta_{\varepsilon r} = \theta_\alpha + \theta_\beta I_{i_{tr}}^p(t), \end{cases} \quad (26)$$

where θ_α and θ_β are constant values. Then \mathcal{V}_k and the desired visible region $\hat{\mathcal{V}}_k$ are described as

$$\begin{cases} \mathcal{V}_k = \left\{ x \in \mathbb{R}^3 \mid \langle x - z_k, \xi_k \rangle \leq \theta_k \right\}, \\ \hat{\mathcal{V}}_k = \left\{ x \in \mathbb{R}^3 \mid \langle x - z_k, \hat{\xi}_k \rangle \leq \hat{\theta}_k \right\}. \end{cases} \quad (27)$$



(a)



(b)

Fig. 7. (a) The heatmap of the target position distribution relative to the tracker on x-y plane. (b) The horizontal distance curve between the tarcker and target in one specific deceleration.



Fig. 8. Our quadrotor platform.

We expect $p(t_k)$ to lie inside $\hat{\mathcal{V}}_k$. To additionally improve visibility, we prefer that $p(t_k)$ be positioned inside \mathcal{V}_{k+1} . Then the visibility constraints are described as

$$\begin{cases} \mathcal{G}_{\hat{\mathcal{V}}} = \cos(\hat{\theta}_k) - \frac{\overrightarrow{p(t_k) - z_k} \cdot \overrightarrow{\hat{\xi}_k}}{\|p(t_k) - z_k\|} \leq 0, & 1 \leq k \leq N_p, \\ \mathcal{G}_{\mathcal{V}} = \cos(\theta_{k+1}) - \frac{\overrightarrow{p(t_k) - z_{k+1}} \cdot \overrightarrow{\xi_{k+1}}}{\|p(t_k) - z_{k+1}\|} \leq 0, & 1 \leq k < N_p. \end{cases} \quad (28)$$

Ultimately, the absolute penalty is written as

$$\mathcal{J}_a^*(\mathbf{c}_j, T_i) = \max\{\mathcal{G}_*(\mathbf{c}_j, t_k), 0\}^3, \star = \{d_l, d_u, \hat{\nu}, \nu\} \quad (29)$$

By solving the optimization problem above, a smooth and collision-free spatial-temporal optimal trajectory is generated.

VI. EXPERIMENTS

A. Simulation Benchmarks

We carry out benchmark comparisons against Ji's [5] work in simulation. The simulated experiments are carried out on a desktop equipped with an Intel Core i7-12700F CPU. We designate another UAV as the target and broadcast its position and yaw angle to the trackers. The initial position of the trackers and the trajectory of the target are identical

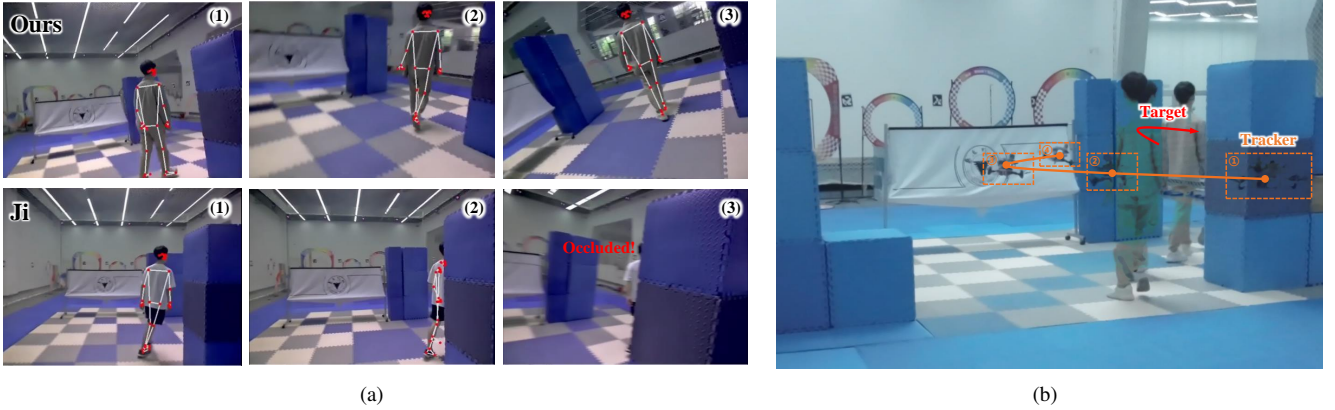


Fig. 9. (a) The camera view of the trackers in one turning scenario. Our tracker can keep good visibility of the target, while Ji's experiences occlusion issues. (b) The trajectory of our tracker during the turning process.

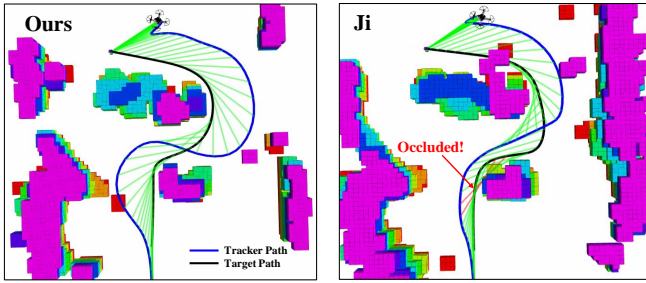


Fig. 10. The tracker's path of the two methods when the target passes a T-shaped intersection.

when benchmarking the two methods. The max velocity and acceleration of the trackers are set to $3m/s$ and $5m/s^2$. Target's max acceleration is $3m/s^2$ and the desired horizontal distance between the tracker and target is set to $[1.6m, 2.4m]$.

First, to benchmark their performance in turning scenarios, the target is maneuvered at various speeds in a dense environment and executes approximately 50 random sharp turns. We count the occlusion time of each tracker, shown in Fig. 6(a). It can be observed that the occlusion time of our method is significantly lower. Even at a high target velocity, our method's failure rate remains under 5%. The performance of our tracker during one specific turn are shown in Fig. 6(b). We can see that as the target approaches the corner, our tracker is able to perceive the turning risk and move away from the obstacle. When the target turns, our tracker correctly predicts its intention and plans an appropriate trajectory accordingly. In contrast, Ji's tracker is occluded during the turn because of ignoring the target intention.

Further benchmarks are conducted in deceleration scenarios. We let the target execute several sudden decelerations at the max speed of $2m/s$ and count target's positions on the x-y plane, shown in Fig 7(a). The horizontal distance curve during one deceleration is shown in Fig. 7(b). Evidently, our tracker is able to maintain a safe distance from the target during decelerations, while Ji's tracker will be too close

to the target. So we can see that our tracker's ability to perceive the target intention significantly improves the safety of tracking.

B. Real-world Experiments

Our quadrotor platform is equipped with an Intel Realsense D435 depth camera for mapping, a monocular camera ($FOV = 90^\circ \times 75^\circ$) for target detection and an Intel NUC-12WSK7 as on-board computer, shown in Fig. 8.

We construct a T-shaped intersection and let the target perform sharp turns at the intersection, because this scene is quite common in real life and poses a great challenge to the tracker. To mitigate the influence of target localization, we broadcast the target's position to the tracker when employing Ji's method. As shown in Fig. 1, when the target makes a turn, its motion prediction path aligns with its intention, and the tracker promptly flies to the side with better visibility. Fig. 9(a) shows the camera view of the two methods during one turning process. It can be observed that our method can keep the target's visibility while Ji's method experiences occlusion issues. From Fig. 10 we can see that as the target approaches the intersection, our tracker has already moved to the position with good visibility, whereas Ji's tracker fails to perceive target intention and can't prepare for the turn in advance. Furthermore, we observe that when the target turns body at the corner, our tracker will execute a significant turn as shown in Fig 9(b), while Ji's tracker turns more slowly. We conduct ten turning tests for both methods, and our method achieves a success rate of 80%, while Ji's method has a success rate of 30%. So we can conclude that tracking becomes more robust when we pay attention to the target intention.

VII. CONCLUSION

In this paper, we incorporate the target intention into aerial tracking planning through novel contributions in intention forecasting and motion prediction. Experimental results demonstrate the safety and robustness of our method. In the future, we will complete other tasks based on aerial tracking, such as videography and rescue.

REFERENCES

- [1] B. Jeon, Y. Lee, and H. J. Kim, "Integrated motion planner for real-time aerial videography with a drone in a dense environment," in *2020 IEEE International Conference on Robotics and Automation (ICRA)*. IEEE, 2020, pp. 1243–1249.
- [2] Z. Han, R. Zhang, N. Pan, C. Xu, and F. Gao, "Fast-tracker: A robust aerial system for tracking agile target in cluttered environments," in *2021 IEEE international conference on robotics and automation (ICRA)*. IEEE, 2021, pp. 328–334.
- [3] Q. Wang, Y. Gao, J. Ji, C. Xu, and F. Gao, "Visibility-aware trajectory optimization with application to aerial tracking," in *2021 IEEE/RSJ International Conference on Intelligent Robots and Systems (IROS)*. IEEE, 2021, pp. 5249–5256.
- [4] N. Pan, R. Zhang, T. Yang, C. Cui, C. Xu, and F. Gao, "Fast-tracker 2.0: Improving autonomy of aerial tracking with active vision and human location regression," *IET Cyber-Systems and Robotics*, vol. 3, no. 4, pp. 292–301, 2021.
- [5] J. Ji, N. Pan, C. Xu, and F. Gao, "Elastic tracker: A spatio-temporal trajectory planner for flexible aerial tracking," in *2022 International Conference on Robotics and Automation (ICRA)*. IEEE, 2022, pp. 47–53.
- [6] Z. Zhang, Y. Zhong, J. Guo, Q. Wang, C. Xu, and F. Gao, "Auto filer: Autonomous aerial videography under human interaction," *IEEE Robotics and Automation Letters*, vol. 8, no. 2, pp. 784–791, 2022.
- [7] J. Kim and D. H. Shim, "A vision-based target tracking control system of a quadrotor by using a tablet computer," in *2013 international conference on unmanned aircraft systems (icuas)*. IEEE, 2013, pp. 1165–1172.
- [8] A. G. Kendall, N. N. Salvapantula, and K. A. Stol, "On-board object tracking control of a quadcopter with monocular vision," in *2014 international conference on unmanned aircraft systems (ICUAS)*. IEEE, 2014, pp. 404–411.
- [9] H. Cheng, L. Lin, Z. Zheng, Y. Guan, and Z. Liu, "An autonomous vision-based target tracking system for rotorcraft unmanned aerial vehicles," in *2017 IEEE/RSJ international conference on intelligent robots and systems (IROS)*. IEEE, 2017, pp. 1732–1738.
- [10] S. Bonnin, T. H. Weisswange, F. Kummert, and J. Schmüderich, "Pedestrian crossing prediction using multiple context-based models," in *17th International IEEE Conference on Intelligent Transportation Systems (ITSC)*. IEEE, 2014, pp. 378–385.
- [11] M. Goldhammer, S. Köhler, K. Doll, and B. Sick, "Camera based pedestrian path prediction by means of polynomial least-squares approximation and multilayer perceptron neural networks," in *2015 SAI Intelligent Systems Conference (IntelliSys)*. IEEE, 2015, pp. 390–399.
- [12] A. Dominguez-Sánchez, M. Cazorla, and S. Orts-Esculano, "Pedestrian movement direction recognition using convolutional neural networks," *IEEE transactions on intelligent transportation systems*, vol. 18, no. 12, pp. 3540–3548, 2017.
- [13] J. Li, Q. Li, N. Chen, and Y. Wang, "Indoor pedestrian trajectory detection with lstm network," in *2017 IEEE International Conference on Computational Science and Engineering (CSE) and IEEE International Conference on Embedded and Ubiquitous Computing (EUC)*, vol. 1. IEEE, 2017, pp. 651–654.
- [14] D. Kulic and E. A. Croft, "Affective state estimation for human–robot interaction," *IEEE transactions on robotics*, vol. 23, no. 5, pp. 991–1000, 2007.
- [15] J. F. P. Kooij, N. Schneider, F. Flohr, and D. M. Gavrila, "Context-based pedestrian path prediction," in *Computer Vision–ECCV 2014: 13th European Conference, Zurich, Switzerland, September 6–12, 2014, Proceedings, Part VI 13*. Springer, 2014, pp. 618–633.
- [16] H. S. Koppula and A. Saxena, "Anticipating human activities using object affordances for reactive robotic response," *IEEE transactions on pattern analysis and machine intelligence*, vol. 38, no. 1, pp. 14–29, 2015.
- [17] A. T. Schulz and R. Stiefelhagen, "A controlled interactive multiple model filter for combined pedestrian intention recognition and path prediction," in *2015 IEEE 18th International Conference on Intelligent Transportation Systems*. IEEE, 2015, pp. 173–178.
- [18] A. Alahi, K. Goel, V. Ramanathan, A. Robicquet, L. Fei-Fei, and S. Savarese, "Social lstm: Human trajectory prediction in crowded spaces," in *Proceedings of the IEEE conference on computer vision and pattern recognition*, 2016, pp. 961–971.
- [19] V. Bazarevsky, I. Grishchenko, K. Raveendran, T. Zhu, F. Zhang, and M. Grundmann, "Blazepose: On-device real-time body pose tracking," *arXiv preprint arXiv:2006.10204*, 2020.
- [20] D. Dolgov, S. Thrun, M. Montemerlo, and J. Diebel, "Practical search techniques in path planning for autonomous driving," *Ann Arbor*, vol. 1001, no. 48105, pp. 18–80, 2008.
- [21] Z. Wang, X. Zhou, C. Xu, and F. Gao, "Geometrically constrained trajectory optimization for multicopters," *IEEE Transactions on Robotics*, vol. 38, no. 5, pp. 3259–3278, 2022.
- [22] S. Liu, M. Watterson, K. Mohta, K. Sun, S. Bhattacharya, C. J. Taylor, and V. Kumar, "Planning dynamically feasible trajectories for quadrotors using safe flight corridors in 3-d complex environments," *IEEE Robotics and Automation Letters*, vol. 2, no. 3, pp. 1688–1695, 2017.
- [23] L. S. Jennings and K. L. Teo, "A computational algorithm for functional inequality constrained optimization problems," *Automatica*, vol. 26, no. 2, pp. 371–375, 1990.